TWO EXTRASOLAR ASTEROIDS WITH LOW VOLATILE-ELEMENT MASS FRACTIONS

M. Jura[a], S. Xu(许偲艺)[a], B. Klein[a], D. Koester[b] & B. Zuckerman[a]

ABSTRACT

Using ultraviolet spectra obtained with the *Cosmic Origins Spectrograph* on the *Hubble Space Telescope*, we extend our previous ground-based optical determinations of the composition of the extrasolar asteroids accreted onto two white dwarfs, GD 40 and G241-6. Combining optical and ultraviolet spectra of these stars with He-dominated atmospheres, 13 and 12 polluting elements are confidently detected in GD 40 and G241-6, respectively. For the material accreted onto GD 40, the volatile elements C and S are deficient by more than a factor of 10 and N by at least a factor of 5 compared to their mass fractions in primitive CI chondrites and approach what is inferred for bulk Earth. A similar pattern is found for G241-6 except that S is undepleted. We have also newly detected or placed meaningful upper limits for the amount of Cl, Al, P, Ni and Cu in the accreted matter. Extending results from optical studies, the mass fractions of refractory elements in the accreted parent bodies are similar to what is measured for bulk Earth and chondrites. Thermal processing, perhaps interior to a snow line, appears to be of central importance in determining the elemental compositions of these particular extrasolar asteroids.

Subject headings: planetary systems – stars, white dwarf

1. INTRODUCTION

Evidence is now compelling that most externally-polluted white dwarfs derive their heavy elements[1] by accretion from tidally-disrupted planetesimals (Debes & Sigurdsson 2002; Jura 2003; Gaensicke et al. 2006; Jura 2008; Farihi et al. 2010; Zuckerman et al. 2010). Here, we report new ultraviolet spectroscopy of two polluted white dwarfs to exploit this uniquely powerful tool to determine the bulk composition of extrasolar asteroids – the building blocks of rocky planets.

[a]Department of Physics and Astronomy, University of California, Los Angeles CA 90095-1562; jura, sxu, kleinb, ben@astro.ucla.edu

[b]Institut fur Theoretische Physik und Astrophysik, University of Kiel, 24098 Kiel, Germany; koester@astrophysik.uni-kiel.de

[1]To avoid the specific connotation of "metals" in the context of planetary physics, we use "heavy elements" to mean all elements heavier than helium.

The composition of extrasolar planets is of great interest and considerable effort has been devoted to studying main-sequence stars with the goal of identifying spectroscopic signatures of accretion of planets (Ramirez et al. 2010; Gonzalez Hernandez et al. 2011; Brugamyer et al. 2011; Schuler et al. 2011). However, because a star's own heavy elements dominate the composition of its photosphere, it is very difficult to determine a planetary contribution to the measured abundances. In contrast, as reviewed by Koester (2009), white dwarfs with effective temperatures less than 25,000 K typically have atmospheres that are nearly pure hydrogen or pure helium and the observed heavy elements usually are the result of external pollution[2]. With the discovery of 17 individual elements within the photosphere of the white dwarf GD 362, it has become clear that we can use these externally-polluted stars to make detailed comparisons of the bulk compositions of extrasolar planetesimals with those of the solar system's terrestrial planets (Zuckerman et al. 2007).

About 94% of bulk Earth's total mass is contained within four dominant elements: O, Mg, Si and Fe (Allegre et al. 2001). Ground-based optical spectra with some additional results from *FUSE*, the *Far Ultraviolet Spectroscopic Explorer*, indicate that these same four species comprise at least 85% of the heavy element mass in six highly polluted white dwarfs (Klein et al. 2010, 2011; Dufour et al. 2010; Vennes et al. 2010; Zuckerman et al. 2010; Farihi et al. 2011; Melis et al. 2011). However, these optical studies incompletely sample important species which only have strong lines in the ultraviolet. We have therefore acquired spectra with the *Hubble Space Telescope* to measure the abundances of additional elements in GD 40 and G241-6, two of the three most heavily polluted DB white dwarfs within 80 pc of the Sun (Jura & Xu 2012). Our ultraviolet data are a substantial improvement over older, lower-resolution data for GD 40 (Friedrich et al. 1999; Wolff et al. 2002); no previous ultraviolet spectroscopy has been performed on G241-6.

GD 40 shows excess infrared continuum emission from a circumstellar dust disk (Jura et al. 2007) that also displays 10 μm silicate emission (Jura et al. 2009). While G241-6 and GD 40 have nearly the same effective temperatures, gravities and abundances of heavy-element pollutants (Zuckerman et al. 2010; Klein et al. 2011), G241-6 does not display an infrared excess (Xu & Jura 2012). Either G241-6's disk is fully gaseous or the parent body has been largely accreted and we are witnessing lingering contamination in the stellar photosphere; heavy elements take longer than 2×10^5 yr to sink below the outer mixing zone (Koester 2009; Klein et al. 2010).

In the standard picture (Wetherill 1990; Armitage 2010), planet-forming disks have well defined radial temperature zones and rocky planets assemble from material in a relatively narrow annulus. Therefore a single condensation temperature can usefully describe the bulk abundances. This picture has been adopted in models for the formation of extrasolar rocky planets (Bond et al.

---

[2]Exceptions include the DQ white dwarfs where carbon is dredged-up from the interior (Koester et al. 1982; Pelletier et al. 1986), "warm" DQ stars where carbon dominates the composition of the photosphere (Dufour et al. 2007), and high-mass white dwarfs where oxygen is dredged-up (Gaensicke et al. 2010). Also, small amounts of C, Al and Si can be supported in the atmospheres of some stars by radiative levitation (Dupuis et al. 2010).

2010); extrasolar planetesimals are expected to be volatile-poor if they form sufficiently close to their host star.

In the solar system, an element's condensation temperature is key in determining its incorporation into a planetesimal. Typically, for the pressure, temperature and presumed composition of the solar nebula, the molecular constituents are computed and the fractional condensation is determined for each compound. For bulk Earth, refractory elements that are incorporated into solids at temperatures above 1100 K are undepleted relative to solar abundances while volatile elements with a condensation temperature less than 1000 K are deficient by factors of as much as 100 or more compared to a solar composition (Allegre et al. 2001). The most primitive meteorites, the CI chondrites, only display depletions relative to solar values of elements with condensation temperatures below 200 K, while the more evolved CV chondrites have depletions by at least a factor of two of elements with a condensation temperature below ∼700 K (Wasson & Kallemeyn 1988).

Previous support for volatile-depletion within extrasolar planetesimals is given by the evidence that carbon is usually deficient (Jura 2006; Farihi et al. 2009). Furthermore, Jura & Xu (2012) found that, in aggregate, planetesimals accreted onto DB white dwarfs have a factor of 10 less H_2O by mass than do CI chondrites, consistent with a scenario where these particular extrasolar rocky bodies were assembled interior to a snow line which, depending upon the gas pressure, is located where the temperature is between 145 K and 170 K (Lecar et al. 2006). By measuring volatile compositions of individual extrasolar asteroids, we can more exactly assess the degree to which they are thermally processed.

The most important volatile elements that might be detected in polluted white dwarf spectra are C, N, and S with 50% condensation temperatures of 40 K, 123 K, and 664 K, respectively (Lodders 2003) because they are expected to be largely contained within CH_4, NH_3 and FeS. Another abundant volatile is oxygen, but this element is special because much of it is incorporated into oxides of refractory elements such as Si and Mg. Typically, there is "leftover" oxygen which does not condense into solids until the system attains a much lower temperature at which point H_2O ice forms.

In Section 2, we report our data acquisition and reduction. In Section 3, we report atmospheric abundances while in Section 4 we infer compositions of the accreted parent bodies. In Section 5, we discuss our results in the context of models for the growth of planetesimals and in Section 6 we present our conclusions.

2. DATA ACQUISITION AND REDUCTION

For both GD 40 and G241-6, we obtained spectra with the G130M grating of the *Cosmic Origins Spectrograph* (COS) during Cycle 18 of the *Hubble Space Telescope* under GO Program 12290. Observations were obtained in the TIME-TAG mode using the 2″5 diameter primary science

aperture (PSA) with a central wavelength of 1300 Å. Data were acquired during 3 spacecraft orbits for each star with a total integration time of 7,740 s for GD 40 and 8,835 s for G241-6. In each orbit, the FP-POS value was set to a different value to minimize the fixed pattern noise in the detector. The spectra extend from 1140 Å to 1440 Å except for a slight gap of $\sim$ 12 Å near 1300 Å; the spectral resolution was $\sim$ 20,000.

The raw COS data were processed with CALCOS pipeline 2.15.4 and then smoothed with a boxcar of five pixels. At most wavelengths, the signal-to-noise ratio for each star is > 25. The final spectra presented here are flux calibrated and in vacuum wavelengths. Because of strong terrestrial day airglow emission from O I between 1300 Å and 1308 Å and from H I near Lyman α (Feldman et al. 2001), we use the *timefilter* module to extract the night time portion of the data and rerun CALCOS to obtain the calibrated spectra for these two spectral intervals. The airglow emission is completely removed at the oxygen lines; however, residual emission remains at Lyman α (Figure 1). Near the edge of the spectrum at 1300 Å, the pipeline reduction becomes somewhat noisy and unreliable (private communication, COS help desk). The COS-measured flux of both stars near 1400 Å is 1.4×10^{-14} erg cm^{-2} s^{-1} Å^{-1}, the same as measured with the GALEX satellite in a broad band centered at 1528 Å.

Similar to the data reduction procedures described in Klein et al. (2010, 2011) and Zuckerman et al. (2010), with IRAF, each absorption line was fit with a Voigt profile and the equivalent width (EW) was derived. For each line, we performed three different measurements and the final EW uncertainty was obtained by adding three factors in quadrature: the standard deviation of the three fits, the average uncertainty of an individual fit to the assumed profile and the uncertainty of the continuum. For marginally blended lines, we used "splot" in IRAF to perform deblending and measure the individual EW. We list in Table 1 the lines with values of the EW greater than 50 mÅ in at least one of our two target stars.

For elements without positive detections, we place upper limits to the EW by measuring the signal-to-noise ratio at the region of its expected strongest line. We calculate the 1 σ uncertainty by dividing the Full Width Zero Intensity by the signal-to-noise ratio. We quote 3σ values for the upper limits to the EWs. In the best-case, this procedure translates to an EW of 24 mÅ, but, for some lines, the upper limit to the EW is 30 mÅ or even 35 mÅ. We validated this procedure by inserting artificial lines into the data.

As expected from ground-based optical spectra, the ultraviolet spectra of GD 40 and G241-6 each exhibit hundreds of photospheric absorption lines, many more than can be found in the older ultraviolet data of GD 40 which had only 1 Å resolution (Friedrich et al. 1999) and a lower signal-to-noise ratio. The EW's of almost all the photospheric lines are less than 200 mÅ and therefore would have been difficult to detect in the older data.

The average heliocentric velocity of the photospheric lines from the COS spectra is 19 km s^{-1} and -23 km s^{-1} for GD 40 and G241-6, respectively. As with the optical data, the dispersion is near 5 km s^{-1} for each star (Klein et al. 2010, 2011). These values are different from the optically-

measured values; Klein et al. (2010) and Zuckerman et al. (2010) reported the velocities of 10 km/s and -28 km/s for GD 40 and G241-6, respectively. The difference between the optical and ultraviolet results can be attributed to the well-known difficulty of measuring absolute velocities with COS to better than 15 km s^{-1} (COS Instrument Handbook). In Figures 1-10, some of the observed spectra are additionally shifted beyond the nominal correction for the heliocentric velocity by as much as $\pm$ 4 km s^{-1} to match more exactly the model spectra.

3.   ABUNDANCE DETERMINATIONS

Our abundance determinations from the ultraviolet data follow closely the procedures described previously for our optical observations (Klein et al. 2010, 2011; Zuckerman et al. 2010). Unless otherwise specified, we use atomic data taken from either VALD[3] or NIST[4] and the model atmosphere parameters listed in Table 2. For GD 40, Bergeron et al. (2011) derive an effective temperature of 14,780 K and log g = 8.13 (cgs units). Following the arguments in Klein et al. (2010) we adopt a temperature of 15,300 K which, however, may be in error by $\sim$ 500 K. Regardless, as shown in Klein et al. (2010, 2011), variations of the effective temperature of 500 K and log g of 0.3 typically lead to changes in the abundances of heavy elements relative to each other by less than 0.1 dex although the abundances relative to He, the dominant gas in the photosphere, can vary by as much as 0.4 dex. Therefore, the uncertainties in our adopted effective temperature and gravity do not lead to any qualitative change in our results. For G241-6, our value of the effective temperature of 15,300 K is nearly equal to the 15,230 K temperature independently derived by Bergeron et al. (2011). For this same star, our value of the gravity of log g = 8.0 is slightly smaller than the value of log g of Bergeron et al. (2011).

To derive abundances, we compare COS data with a model atmosphere to find the best fit to each line profile and EW. For all detailed comparisons displayed below, we convolve the model predictions with the COS line spread function (Kriss 2011). From the measured EW of each individual line, we compute an abundance estimate. For each element, we then average, weighted by the quality of the data and atomic parameters, over each individual value to derive the ultraviolet-determined abundance that best fits all of an element's spectral lines.

The error determinations arise from scatter in the measurement of the equivalent widths and uncertainties in the models and atomic parameters. As demonstrated in Klein et al. (2010), the abundance uncertainties propagated from EW determination are much less than the standard deviation of the abundance determined from different lines. As a result, the final abundance uncertainty for each element is derived from the internal dispersion of all its lines. Because of modeling uncertainties, we assume a minimum error of 0.10 dex in all of our "final" abundances –

---

[3] http://vald.astro.univie.ac.at/~vald/php/vald.php?docpage=usage.html

[4] http://physics.nist.gov/PhysRefData/ASD/Html/verhist.shtml

including those with only optical determinations.

Our final abundance for each element is determined by combining our previous optical studies (Klein et al. 2010; Zuckerman et al. 2010) with our current COS analysis; these results are provided in Tables 3 and 4. Below, we discuss each element in detail. Representative data are shown in Figures 1-10 where we also display the predictions from models employing the final set of abundances.

3.1. Potential Interstellar Lines

Ultraviolet spectra of nearby stars display many interstellar absorption lines from species in the ground electronic state (Spitzer & Jenkins 1975). Using *FUSE* to perform a survey of white dwarfs within 200 pc of the Sun, Lehner et al. (2003) found, as expected, that interstellar absorption lines are pervasive. Therefore, although both GD 40 and G241-6 lie within the local interstellar bubble where the density is relatively low, their ultraviolet spectra must possess interstellar absorption lines. Extensive optical surveys of the local interstellar gas show that it is patchy (Welsh et al. 2010), and we cannot predict its amount. We therefore estimate the importance of interstellar lines by considering a likely range of absorption line strengths. A convenient tabulation of the equivalents widths of interstellar absorption lines has been presented for α Vir (York & Kinahan 1979), a star whose distance of 77 pc suggests that it should experience roughly comparable amounts of interstellar absorption as GD 40 and G241-6. The interstellar lines in our target white dwarfs almost certainly are weaker than those measured in ζ Oph (Morton 1975), a star with famously strong interstellar lines whose distance of 112 pc puts it outside the local bubble. In Table 1, in addition to listing the strengths of the photospheric lines of GD 40 and G241-6 from COS data, we list the measurements from the *Copernicus* satellite of EWs in the spectra of α Vir and ζ Oph whose narrow lines must be interstellar because the stars are rapidly rotating.

Another way to independently determine whether a line is interstellar or photospheric is to measure its radial velocity, since these two types of lines usually have different velocities. Unfortunately, for GD 40 these two velocities are almost the same so this method fails to discern interstellar lines. The radial velocity offset between interstellar and photospheric lines for G241-6 is about 20 km s^{-1} and can be used to identify interstellar features. The offsets for C and N are provided in the captions to Figures 2 and 3.

3.2. Hydrogen

Even though as shown in Figure 1 there is substantial residual airglow emission, we have used the COS "night-time" observations to derive upper bounds to the column density of atomic hydrogen, N(H), from the Lyman α line, H I 1216 Å. Unfortuantely, we cannot easily determine how much of the line is interstellar and how much is photospheric. For GD 40, the star with the

stronger Lyman α line, if the hydrogen is entirely photospheric, then in the usual notation where [X]/[He] denotes log $n(X)/n(He)$, we derive [H]/[He] = -5.1, approximately a factor of 10 greater than found from Hα (Klein et al. 2010). If [H]/[He] = - 6.14 as determined from the optical data, then following Bohlin (1975), we find N(H) = 1.0×10^{20} cm^{-2}, approximately a factor of 10 greater than values of N(H) for stars 70 pc from the Sun (Lehner et al. 2003). Therefore, it is likely that the Lyman α line is primarily photospheric. It is possible that the broad, weak Hα line was not well measured in the Keck HIRES echelle spectrum which is difficult to flatten (Klein et al. 2010). However, Voss et al. (2007) also report a very weak Hα absorption line and derived [H]/[He] = -6.02. Bergeron et al. (2011) report [H]/[He] = -6.1, but with an uncertainty of 1.0 dex because the line is weak and difficult to measure. Our final estimate of the abundance reported in Table 3 has a large uncertainty.

We hope to reconcile the discrepancy between the optical and ultraviolet results for photospheric hydrogen in GD 40 in future studies; for now it is mystery. Fortunately this factor of 10 uncertainty in the hydrogen abundance does not materially affect the overall structure of the model atmosphere, so the abundance determinations for other elements are unaffected.

For G241-6, from the lack of Hα absorption, Zuckerman et al. (2010) report [H]/[He] < -6.1 while Bergeron et al. (2011) report an upper limit to [H]/[He] of -5.43. If the Lyman α line is entirely photospheric in origin, then [H]/[He] = -5.6, in disagreement with the upper limit from Zuckerman et al. (2010). If, however, [H]/[He] = -6.1 in the photosphere, then, as illustrated in Figure 1, N(H) = 3×10^{19} cm^{-2}. Given that interstellar nitrogen lines detected toward this star are stronger than those measured for α Vir, it is plausible that the interstellar hydrogen column density could approach this value of 3×10^{19} cm^{-2}. If so, then there is no disagreement between the measurement of [H]/[He] derived from the ultraviolet and the upper bound derived from the optical.

3.3. Carbon

The ultraviolet lines of C I and C II that are accessible in our COS data are subject to interstellar contamination because they arise either from the ground state or a very low-lying energy level. In Figure 2, we display the comparison between our data and models for GD 40 and G241-6 for the spectral interval 1327 Å to 1338 Å. In both stars, we see C II absorption at 1334.53 Å and 1335.71 Å. However, neither interstellar nor photospheric absorption from C I is detected.

In Table 1, the C II lines toward GD 40 are somewhat stronger than even in ζ Oph. Furthermore, the line at 1335.71 Å arises from an excited fine structure level (see column 2 in Table 1) which is fully populated according to its statistical weight in a stellar photosphere but not so in the interstellar medium where the density is vastly lower. Consequently, an interstellar line at 1335.71 Å is almost always weaker than the line at 1334.53 Å. In view of this consideration, it is likely that the C II lines toward GD 40 are largely photospheric with an abundance of [C]/[He] = -7.8. Our

upper bounds to the CI lines near 1277 Å and 1328 Å are consistent with this result.

For G241-6, it appears that the CII line at 1334.53 Å is largely interstellar because it is offset from the photospheric velocity and because it is substantially stronger than the CII 1335.71 Å line. If C II 1335.71 Å is entirely photospheric, then [C]/[He] = -8.5. Because the line is likely at least partly interstellar, we conclude that this value of the abundance is only an upper limit. Our upper bounds to the CI lines near 1277 Å and 1328 Å are consistent with this result.

3.4.   Nitrogen

The accessible photospheric lines of N I at 1199.55 Å, 1200.22 Å and 1200.71 Å all arise from the ground state and are strong in the interstellar medium. A further difficulty is that these lines can be blended with photospheric Fe II 1199.67 Å,1200.24 Å and 1200.75 Å. As shown in Figure 3, the Fe lines dominate this spectral region, and there is no evidence for any nitrogen lines in the spectrum of GD 40; we derive [N]/[He] < -8.8. For G241-6, the observed lines probably arise from interstellar absorption because their wavelengths are offset and from what is expected in the stellar rest frame and, instead, agree with the offset of the likely interstellar line at C II 1334.53 Å. There is no evidence for photospheric nitrogen; we derive an upper limit of [N]/[He] < -8.9.

3.5.   Oxygen

We detect O I 1152.15 Å and 1217.65 Å in both stars; the data are shown in Figures 4 and 1. These lines must be photospheric because they arises from excited electronic states. Using night-time data only to avoid day glow emission, we also detect O I 1302.17 Å, 1304.86 Å and 1306.03 Å; these lines are shown in Figure 5. Because the O I 1302.17 Å line lies near the edge of the array, the data are especially noisy and uncertain in its blue wing (private communication, COS help desk). The two longer wavelength O I lines are blended with lines of Si II. Because of these problems, we do not employ any of the three lines near 1302 Å in our abundance determination

3.6.   Aluminum

The only line that we have used for the abundance determination for this element is Al II 1191.80 Å which cannot be interstellar because it arises from an excited energy level. The fits to the data are shown in Figure 6. As shown in Figure 1, we have apparently detected Al II 1211.90 Å in GD 40, but this line is blended with a feature from Fe II, we do not attempt to use these data to infer the aluminum abundance.

3.7. Silicon

We have detected numerous ultraviolet lines of Si II and one line of Si III in both GD 40 and G241-6; results are shown in Figures 5-8. For GD 40, the Si II data cannot be consistently fit. The model with our final abundance still under-predicts the strengths of the lines near 1260 Å and 1350 Å, but as reported in Klein et al. (2010) would over-predict the optical EWs. The lines near 1194 Å are well fit with the compromise "final" value of [Si]/[He] given in Table 3 which is larger than previously reported by Klein et al. (2010) by 0.32 dex. In contrast, we find a more self-consistent fit of all the Si lines for G241-6 with only a 0.16 dex increase in [Si]/[He]. Independently, in GD 61, a comparably externally-polluted DB white dwarf, the optical and ultraviolet determinations agree to within 0.15 dex (Farihi et al. 2011; Desharnais et al. 2008). Bautista et al. (2009) have re-examined the oscillator strengths of Si II, and while their values for the ultraviolet lines are close to those employed in this paper, their recommended values for the optical lines are about 0.3 dex weaker than we previously used and thus accounting for much of the discrepancy between the optical and ultraviolet abundance determinations for GD 40. The abundance difference between Si and Mg discussed in detail by Klein et al. (2010) for GD 40 is still present with our current analysis but is significantly less pronounced than previously reported.

3.8. Phosphorus

Unequivocal detections of three P II lines for both stars are shown in Figure 4. The stellar abundance determinations in Tables 3 and 4 are secure.

3.9. Sulfur

As shown in Figure 7, we have certainly detected the S II doublet of 1204.27 Å and 1204.32 Å for G241-6 and perhaps for GD 40. These lines must be photospheric. For G241-6, we also detected the lines at 1253.81 Å and 1259.52 Å (Figure 8); for GD 40, detections of the these two lines is marginal. We also have detected S I 1433.28 toward G241-6 which is unlikely to be interstellar. The photospheric abundance determination of sulfur in G241-6 is secure; it is tentative in GD 40.

3.10. Chlorine

As shown in Figure 9, we only report upper limits to Cl I 1347.24 Å.

3.11.   Magnesium, Calcium, Titanium, Chromium, Manganese, Iron

We detected lines of Mg, Ca, Ti, Cr, Mn and Fe in the COS spectra. Our measurements for Ti are not presented in Table 1 because they are all weaker than 50 mÅ. For all of these elements, our final abundance determination largely is based upon our previous results. Except for Ca, the abundances determinations agree within the errors with those determined from the optical (Klein et al. 2010; Zuckerman et al. 2010). Examples of the model fits for Fe and Mn are shown in Figures 2-4, 6-8 and 10. For Ca, the only lines in the ultraviolet have poorly determined atomic parameters; they imply a significantly lower Ca abundance than derived from optical data. Given the excellent fit to numerous optical lines, we do not reassess the abundance of this element.

3.12.   Nickel

We display detections of photospheric Ni in Figures 2 and 4. The potentially interstellar Ni lines reported in Table 1 are so much stronger than observed in ζ Oph that we assume that they originate in the photosphere and as-such, they are included in our abundance determination.

3.13.   Copper, Germanium, Gallium

We display the spectra near the Cu II 1358.77 Å line in Figure 10. The line appears at the 3σ level in the spectrum of GD 40, and is at most marginally detected; we can only place an upper bound to the line in G241-6. We have searched for lines at 1404.12 Å and 1237.07 Å for Ge and Ga, respectively. They are undetected and not displayed here; the upper limits to the abundances are reported in Tables 3 and 4.

4.   PARENT BODY COMPOSITIONS

Having determined the atmospheric abundances, we now proceed to estimate the composition of the accreted parent bodies. Because different elements gravitationally settle through the white dwarf's outer mixing zone at different rates, the relative abundances in the photosphere may not be the same as the relative abundances in the asteroidal parent body. Koester (2009) described three phases of an accretion event. The first phase is a build-up of pollution after the initial creation of a circumstellar disk derived from the tidal-disruption of an asteroid. During this phase, which has a duration of approximately one settling time, the photospheric abundances are the same as those in the parent body. For both GD 40 and G241-6, this phase has a duration of 2×10^5 yr. During the second phase, there is an approximate steady state where the rate of accretion from the disk is balanced by the loss at the bottom of the outer mixing zone. During this phase the concentration of each individual element in the photosphere is determined by a balance between its

accretion rate and its settling time; derivation of parent body abundances must take this effect into account. The duration of this phase depends upon the mass of the parent body. The estimated steady state accretion rates for GD 40 and G241-6 are 2×10^9 and 3×10^9 g s^{-1} (Klein et al. 2010; Zuckerman et al. 2010). Ceres, the most massive asteroid in the solar system, has a mass of 9.1×10^{23} g (Baer et al. 2011), and it is therefore imaginable that this phase could have a duration of as much as 10^7 yr, but this is extremely uncertain. As listed in Table 5, the inferred minimum mass of the asteroid accreted onto GD 40 of 3.8×10^{22} g, slightly revised from the value of 3.6×10^{22} g in Klein et al. (2010), is much less than the mass of Ceres. If the accretion from the disk varies with time (Rafikov 2011), it may be better described to be in a quasi-steady state instead of an exact steady state. In this case, the estimated mass fractions may be uncertain by as much as a factor of two (Jura & Xu 2012). After the disk is fully accreted, there is a final decay phase where the light elements should dominate the photospheric composition since the heavy elements sink more quickly. The duration of this final phase is on the order of a few settling times, or, for GD 40 and G241-6, $\sim 5 \times 10^5$ yr.

Because we are largely focused upon the upper limit to the abundances of the volatile elements and because carbon and nitrogen have particularly long settling times, it is most conservative to assume that the systems are in the "build-up" phase because this is when we would infer the highest fractional abundances for the volatiles. If, instead, the system is in a steady state or declining phase, we overestimate the fraction of mass carried in the lighter elements and underestimate the fraction of mass carried in the heavier elements. According to Klein et al. (2010), the difference between derived mass fractions between the build-up phase and the steady state phase is at most a factor of 1.6, not enough to qualitatively change our conclusions. If a system is in the declining phase, then the correction to the derived mass fraction of a heavy element such as Ni for gravitational settling can, in principle, be larger than a factor of 10 (Koester 2009).

We display in Figures 11-13 the relative abundances listed in Table 5. Because we have a comprehensive suite of abundances in the atmospheres of GD 40 and G241-6, we follow standard analysis of solar system objects and display the fraction of the total mass of the parent body carried by each element.

We see in Figure 11 that the two elements with 50% condensation temperatures less than 150 K, well inside the snow line (Lecar et al. 2006), are significantly depleted in the parent bodies accreted onto GD 40 and G241-6 relative to the "adjusted sun" and CI chondrites. In contrast, we see in Figures 12-13 that the elements with condensation temperatures greater than 1000 K have mass fractions roughly similar to bulk Earth and CI and CV chondrites. Sulfur with an intermediate 50% condensation temperature of 664 K is heavily depleted in GD 40 but undepleted in G241-6.

5. DISCUSSION

In the usual models for their formation in a disk orbiting a central star, rocky planets grow within a radial annulus. The temperature within this annulus controls the material which is incorporated into solids and therefore, ultimately, the chemical composition of a planet (Armitage 2010). In this picture, there is a snow line, and planets formed interior to this demarcation have little ice. As a first approximation, the abundances within the rocky bodies in the solar system can be explained by this scenario. For example, based solely on solar abundances, carbon should be one of the most abundant elements within a rocky planet. However, in a cosmochemical environment, it is highly volatile and strongly depleted both in the inner solar system (Lee et al. 2010) and in extrasolar asteroids (Jura 2006). Similarly, water-ice is much more abundant in the outer solar system than in the inner solar system (Jewitt et al. 2007).

The depletions of C and S in the parent body accreted onto GD 40 are similar to those of bulk Earth while the upper bound of N in the accreted material is consistent with bulk Earth's low fractional mass of this element. Also, the abundances of the refractories are mostly similar to those in bulk Earth except for an unexplained enhancement of Ca and possibly Ti. Therefore, the formation pathway of the parent body that orbited GD 40 may have been analogous to the formation of Earth. Although C and N are substantially depleted in the parent body accreted onto G241-6, the solar abundance of S suggests that the material condensed at a temperature less than 600 K. Therefore, the formation route of the parent body that orbited this star may have been more similar to that of the CV chondrites. The volatiles deficiencies in GD 40 and G241-6 seem to be part of a more general pattern of the parent bodies accreted onto DB white dwarfs in aggregate likely having formed interior to a snow line (Jura & Xu 2012).

Although similar, the abundances of GD 40 and G241-6 are not identical. As seen in Table 5, while the dominant lighter elements – O and Mg – have nearly the same abundance, the elements as heavy or heavier than Ca are all more abundant in GD 40 by as much as a factor of 2.5. A natural explanation of this difference is that accretion onto G241-6 has effectively stopped and that we are now witnessing a system in a decaying phase where the heavy elements gravitationally settle before the lighter elements. This scenario is consistent with GD 40's possession of a dust disk and the absence of any circumstellar dust orbiting G241-6. Therefore, our "conservative" approach in assuming that G241-6 is in the "build-up" phase may overestimate the mass fractions of the relatively light volatiles, but it correspondingly may underestimate the mass fractions of the relatively heavy refractories. Sulfur and silicon have nearly the same atomic weight and gravitationally settle at nearly the same speed. As illustrated in the modeling of Jura & Xu (2012), the imputed mass fraction carried by silicon – intermediate in mass between oxygen and iron – is approximately constant during an episode where the accretion rate varies by more than a factor of 10. Consequently, the inferred sulfur mass fraction is insensitive to whether the system is a build-up or steady-state phase. Even if G241-6 is in a final, declining phase, the likely corrections to the relative abundances of the heavy elements are approximately a factor of two; such adjustments would not lead to a qualitative change in our analysis.

We now briefly assess whether during either star's high-luminosity Asymptotic Giant Branch evolution prior to becoming a white dwarf, the composition of the asteroids was dramatically altered by sublimation and the consequent loss of volatile elements. According to idealized calculations (Jura & Xu 2010), less than half of any initial internal H_2O is likely to be lost during such a phase by an asteroid with a radius greater than 60 km. The parent body accreted onto GD 40 had a radius of at least 120 km (Klein et al. 2010), and therefore sublimation during the pre-white dwarf evolution of the star is unlikely to explain the deficiency of volatiles in the accreted asteroid. Because GD 40 has an infrared excess, it is likely that a single, large asteroid is responsible for the observed pollution; otherwise the dust particles in the disk likely would have been destroyed by mutual collisions (Jura 2008). For G241-6, a similarly large mass is required to explain the observed pollution and probably the pollution was delivered by one large parent body (Klein et al. 2011). It seems plausible that the inferred deficiencies of volatiles were established when the planetesimals formed. Another possibility is that ∼100 km asteroids are differentiated because of substantial heating by radioactive elements (Young et al. 2003). Because the source of ^{26}Al – the primary source of heating (Ghosh& McSween 1998) – in the early solar system is unknown (Tatischeff et al. 2010), it is uncertain how to compute the thermal evolution in extrasolar planetary systems. The degree to which complex, differentiated asteroids with porosity and hydrated minerals can retain their water and other volatiles is unknown and needs to be addressed in future models.

In the parent bodies accreted onto GD 40 and G241-6, a simple thermal processing model can explain the bulk compositions. However, it is most unlikely that all extrasolar asteroids are volatile depleted; Koester et al. (2011) report that a suite of older DZ white dwarfs have, on average, nearly solar sodium abundance. This element has a 50% condensation temperature of 958 K (Lodders 2003) and is deficient relative to solar in bulk Earth (Allegre et al. 2001). Possibly these stars with cooling ages near 2 Gyr are polluted by a different class of planetesimal than GD 40 and G241-6 which have cooling ages near 0.2 Gyr (Bergeron et al. 2011). Elaboration of dynamic models for the orbital perturbations of planetesimals such as those computed by Bonsor et al. (2011) or Debes et al. (2012) may allow us to determine when to expect accretion of volatile-rich or volatile-poor planetesimals.

Besides thermal processing, other processes such as differentiation may also be important (Klein et al. 2010; Melis et al. 2011; Zuckerman et al. 2011) in determining the composition of extrasolar asteroids. It is most valuable in testing models for planetesimal formation and evolution to measure mass fractions of as many different elements as possible. As summarized by Zuckerman et al. (2011), seven white dwarfs have been found to be polluted by at least eight different elements. Future studies of such extensively polluted white dwarfs may elucidate different evolutionary pathways taken by extrasolar planetesimals.

6. CONCLUSIONS

We have found in the white dwarfs GD 40 and G241-6 that two highly volatile elements – carbon and nitrogen – comprise only a small fraction of the mass in the accreted parent bodies. The deficiency of these two volatiles parallels what is measured for bulk Earth and previous studies showing that in aggregate, there was relatively little water-ice embedded in the ensemble of planetesimals accreted onto nearby externally-polluted white dwarfs with helium-dominated atmospheres Sulfur is significantly depleted in GD 40 but not G241-6. In contrast, elements with condensation temperatures greater than 1000 K have mass fractions similar to those measured in bulk Earth and chondrites. This contrast between volatiles and refractories is consistent with scenarios where the composition of a planetesimal is strongly dependent upon the radial location in the disk where it was formed.

REFERENCES

Allegre, C., Manhes, G., & Lewin, E. 2001, Earth Planet. Sci. Letters, 185, 49

Armitage, P. 2010, Astrophysics of Planet Formation (Cambridge University Press: Cambridge)

Baer, J., Chesley, S. R., & Matson, R. D. 2011, AJ, 141, 143

Bautista, M.A., Quinet, P., Palmeri, P., Badnell, N. R., Bunn, J., & Arav, N. 2009, A&A, 508, 1527

Bergeron, P. et al. 2011, ApJ, 737, 28

Bohlin, R. C. 1975, ApJ, 200, 402

Bond, J., C., O'Brien, D. P., & Lauretta, D. S. 2010, ApJ, 715, 1050

Bonsor, A., Mustill, A. J., & Wyatt, M. C. 2011, MNRAS, 414, 930

Brugamyer, E., Dodson-Robinson, S. E., Cochran, W. D., & Sneden, C. 2011, ApJ, 738. 97

Debes, J. H., & Sigurdsson, S. 2002, ApJ, 572, 556

Debes, J. H., Walsh, K. J., & Stark, C. 2012, ApJ, 747, 148

Desharnais, S., Wesemael, F., Chayer, P., Kruk, J. W., & Saffer, R. A. 2008, ApJ, 672, 540

Dufour, P., Liebert, J., Fontaine, G., & Behara, N. 2007, Nature, 450, 522

Dufour, P., Kilic, M., Fontaine, G., et al. 2010, ApJ, 719, 803

Dupuis, J., Chayer, P., & Henault-Grunet, V. 2010, in 17th European White Dwarf Workshop, AIP Conference 1273, K. Werner & T. Rauch , eds., (American Institute of Physics), 412

Farihi, J., Barstow, M. A., Redfield, S., Dufour, P., & Hambly, N. C. 2010, MNRAS, 404, 2123

Farihi, J., Brinkworth, C. S., Gaensicke, B. T., et al. 2011, ApJ, 728, L8

Farihi, J., Jura, M., & Zuckerman, B. 2009, ApJ, 694, 805

Feldman, P. D., Sahnow, D. J., Kruk, J. W., Murphy, E. W., & Moos, H. W. 2001, J. Geophys. Res., 106, 8119

Friedrich, S., Koester, D., Heber, U., Jeffery, C. S., & Reimers, D. 1999, A&A, 350, 865

Gaensicke, B., T., Koester, D., Girven, J., Marsh, T. R., & Steeghs, D. 2010, Science, 327, 188

Gaensicke, B. T., Marsh, T. R., Southworth, J., & Rebassa-Mansergas, A. 2006, Science, 314, 1908

Ghosh, A., & McSween, H. Y. 1998, Icarus, 134, 187

Gonzalez Hernandez J. I., Israelian, G., Santos, N. C., Sousa, S., Delgado-Mena, E., & Udry, S. 2011, IAU Symp. 276, 422

Jewitt, D., Chizmadia, L., Grimm, R., & Prialnik D. 2007, in Protostars and Planets V, B. Reipurth, D. Jewitt & K. Keil, eds., (University of Arizona Press: Tucson), 863

Jura, M. 2003, ApJ, 584, L91

Jura, M. 2006, ApJ, 653, 613

Jura, M. 2008, AJ, 135, 1785

Jura, M., Farihi, J., & Zuckerman, B. 2007, ApJ, 663, 1285

Jura, M., Farihi, J., & Zuckerman, B. 2009, AJ, 137, 3191

Jura, M., & Xu, S. 2010, AJ, 140, 1129

Jura, M., & Xu, S. 2012, AJ, 143, 6

Klein, B., Jura, M., Koester, D., Zuckerman, B., & Melis, C. 2010, ApJ, 709, 650

Klein, B., Jura, M., Koester, D., & Zuckerman, B. 2011, ApJ, 741, 64

Koester, D. 2009, A&A, 498, 517

Koester, D., Girven, J., Gaensicke, B. T., & Dufour, P. 2011, A&A, 530, 114

Koester, D., Weidemann, V., & Zeidler, E.-M. 1982, A&A, 116, 147

Kriss, G. A. 2011 Improved Medium Resolution Line Spread Function for COS FUV Spectra, in COS Instrument Science Report

Lecar, M., Podolak, M., Sasselov, D., & Chiang, E. 2006, ApJ, 640, 1115

Lee, J.-E., Bergin, E. A., & Nomura, H. 2010, ApJ, 710, L21

Lehner, N., Jenkins, E. B., Gry, C., Moos, H. W., Chayer, P., & Lacour, S. 2003, ApJ, 595, 858

Lodders, K. 2003, ApJ, 591, 1220

Melis, C., Farihi, J, Dufour, P., et al. 2011, ApJ, 732, 90

Morton, D. C. 1975, ApJ, 197, 85

Pelletier, C., Fontaine, G., Wesemael, F., Michaud, G., & Wegner, G. 1986, ApJ, 307, 242

Rafikov, R. 2011, MNRAS, 416, L55

Ramirez, I., Asplund, M., Baumann, P., Melendez, J., & Bensby, T. 2010, A&A, 521, 33

Schuler, S. C., Flateau, D., Cunha, K., King, J. R., Ghezzi, L., & Smith, V. V. 2011, ApJ, 732, 55

Spitzer, L., & Jenkins, E. B. 1975, ARA&A, 13, 133

Tatischeff, V., Duprat, J., & de Sereville, N. 2010, ApJ, 714, L26

Tayal, S. S. & Zatsarinny, O. 2010, ApJS, 188, 32

Vennes, S., Kawka, A., & Nemeth, P. 2010, MNRAS, 404, L40

Voss, B., Koester, D., Napiwotzki, R., Christlieb, N., & Reimers, D. 2007, A&A, 470, 1079

Wasson, J. D., & Kallemeyn, G. W. 1988, Phil. Trans. R. Soc. A., 325, 535

Welsh, B. Y., Lallement, R., Vergely, J.-L., & Raimond, S. 2010, A&A, 510, 54

Wetherwill, G. 1990, Ann. Rev. Earth & Planet. Sci., 18, 205

Wolff, B., Koester, D., & Liebert, J. 2002, A&A, 385, 995

Xu, S., & Jura, M. 2012, ApJ, 745, 88

York, D. G., & Kinahan, B. 1979, ApJ, 228, 127

Young, E. D., Zhang, K. K., & Schubert, G. 2003, Earth & Planetary Sci. Lett., 213, 249

Zuckerman, B., Koester, D., Melis, C., Hansen, B., & Jura, M. 2007, ApJ, 671, 872

Zuckerman, B., Koester, D., Dufour, P. et al. 2011, ApJ, 739, 101

Zuckerman, B., Melis, C., Klein, B., Koester, D., & Jura, M. 2010, ApJ, 722, 725

Table 1 – Measured Equivalent Widths

Line	χ (eV)	GD 40 W_λ(mÅ)	G241-6 W_λ(mÅ)	α Vir[a] W_λ (mÅ)	ζ Oph[b] W_λ(mÅ)	Comment
H I 1215.67	0.000	5700^c (570)	4000^c (400)	<2130	16700	
C II 1334.53	0.000	201 (10)	214 (11)	112.1	189	
C II 1335.71	0.008	212 (11)	127 (10)	62.6	140	
N I 1199.55	0.000		113 (13)	69.8	146	
N I 1200.22	0.000		134 (12)	67.1	131	
N I 1200.71	0.000		147 (12)	56.2	133	
O I 1152.15	1.967	540 (19)	448 (18)			
O I 1217.65	4.190	51 (25)	76 (22)			blend
O I 1302.17	0.000	1130 (166)	966 (63)	89	201	edge
O I 1304.86	0.020	761 (169)	508 (56)	< 0.7	< 3.9	blend
O I 1306.03	0.028	578 (49)	423 (46)	< 0.7	< 4.0	blend
Mg II 1239.93	0.000	151 (11)	146 (12)	1.0	18.7	
Mg II 1240.94	0.000	112 (10)	94 (10)	0.2	13.2	
Al II 1191.81	4.659	68 (9)	< 60			
Si II 1190.42	0.000	1322 (28)	846 (29)	66.1	132	
Si II 1193.29	0.000	1182 (99)	1127 (158)		147	
Si II 1194.50	0.036	2587 (88)	1744 (104)	1.0	14.3	
Si II 1197.39	0.036	1180 (37)	610 (18)		4.8	
Si II 1223.90	5.323	132 (17)	118 (18)			u
Si II 1224.25	5.323	132 (18)	131 (13)			u, blend
Si II 1224.97	5.323	53 (21)	52 (15)			u
Si II 1226.80	0.098	199 (61)	189 (31)			u, blend
Si II 1226.98	0.098	178 (40)	192 (34)			u, blend
Si II 1227.60	5.345	292 (21)	245 (14)			u
Si II 1228.74	5.323	422 (29)	499 (24)			u, blend
Si II 1229.38	5.345	425 (26)	380 (18)			u
Si II 1246.74	5.310	141 (18)	115 (12)			
Si II 1248.43	5.323	193 (13)	166 (10)			
Si II 1250.09	6.858	125 (21)	134 (26)			u, blend
Si II 1250.44	6.859	226 (18)	296 (63)			u

Table 1 – Continued

Line	χ	GD 40	G241-6	α Vir[a]	ζ Oph[b]	
	(eV)	W_λ(mÅ)	W_λ(mÅ)	W_λ (mÅ)	W_λ(mÅ)	Comment
Si II 1251.16	5.345	244 (15)	176 (15)			u
Si II 1260.42	0.000	2765 (85)	2178 (96)	88.5	170	
Si II 1264.74	0.036	5542 (270)	4676 (77)	0.3	15.4	
Si II 1304.37	0.000	614 (49)	500 (46)	59.9	132	blend
Si II 1309.28	0.036	1039 (45)	813 (35)		< 4	
Si II 1346.88	5.323	157 (15)	121 (15)			
Si II 1348.54	5.310	173 (13)	133 (14)			
Si II 1350.07	5.345	284 (25)	265 (14)			
Si II 1352.64	5.323	186 (22)	144 (13)			
Si II 1353.72	5.345	162 (20)	134 (13)			
Si III 1206.50	0.000	1163 (35)	994 (33)	58.7	123	u
P II 1154.00	0.058	82 (21)	59 (14)			
P II 1159.09	0.058	17 (7)	< 30			
P II 1249.83	1.101	86 (18)	41 (9)			
S I 1425.03	0.000	< 37	78 (21)			
S II 1204.28[d]	1.845	36 (11)	98 (13)			
S II 1250.58	0.000	blend	84 (18)	20.1	100	
S II 1253.81	0.000	37 (10)	159 (12)	30.4	106	
S II 1259.52	0.000	< 38	93 (20)	49.2	112	blend
Ca II 1432.50	1.692	130 (32)	< 38			
Ca II 1433.75	1.700	90 (14)	54 (9)			
Cr II 1434.98	1.483	57 (12)				
Cr II 1435.20	1.506	< 36				

Table 1 – Continued

Line	χ	GD 40	G241-6	α Vir[a]	ζ Oph[b]	
	(eV)	W_λ(mÅ)	W_λ(mÅ)	W_λ (mÅ)	W_λ(mÅ)	Comment
Fe II 1143.23	0.000	279 (37)	97 (21)	< 2	38	edge
Fe II 1144.94	0.000	240 (23)	209 (24)			
Fe II 1146.83	0.107	< 50	< 50			blend
Fe II 1146.95	0.048	79 (26)	< 50			blend
Fe II 1147.41	0.083	275 (50)	150 (34)			blend
Fe II 1148.08	0.107	182 (35)	271 (90)			blend
Fe II 1148.28	0.048	173 (44)	288 (27)			blend
Fe II 1149.59	0.121	82 (22)	60 (21)			
Fe II 1150.29	0.083	51 (16)	< 50			blend
Fe II 1150.47	0.121	89 (18)	88 (21)			blend
Fe II 1150.69	0.083	67 (14)	< 38			blend
Fe II 1151.15	0.083	127 (20)	87 (14)			
Fe II 1154.40	0.121	125 (34)	48 (13)			blend
Fe II 1159.34	0.986	57 (17)	48 (13)			blend
Fe II 1168.49	2.807	69 (18)	49 (14)			blend
Fe II 1169.19	0.986	63 (17)	< 30			blend
Fe II 1175.68	0.232	99 (22)	< 30			blend
Fe II 1183.83	0.986	68 (14)	44 (11)			
Fe II 1187.42	0.986	62 (12)	42 (11)			blend
Fe II 1192.03	1.040	68 (25)	50 (13)			blend
Fe II 1198.93	2.635	65 (13)	41 (12)			
Fe II 1267.42	0.048	124 (18)	54 (14)			blend
Fe II 1271.98	0.083	104 (16)	54 (13)			
Fe II 1272.61	0.083	86 (13)	44 (13)			
Fe II 1275.14	0.107	58 (9)	32 (7)			
Fe II 1275.78	0.107	94 (10)	80 (10)			
Fe II 1277.64	0.121	136 (12)	93 (12)			

Table 1 – Continued

Line	χ	GD 40	G241-6	α Vir[a]	ζ Oph[b]	
	(eV)	W_λ(mÅ)	W_λ(mÅ)	W_λ (mÅ)	W_λ(mÅ)	Comment
Fe II 1311.06	4.076	50 (11)	< 40			
Fe II 1358.94	3.245	44 (16)	< 40			blend
Fe II 1361.37	1.671	77 (12)	64 (9)			
Fe II 1364.58	3.267	128 (11)	38 (10)			blend
Fe II 1371.02	2.635	91 (11)	68 (12)			
Fe II 1372.29	1.695	50 (10)	40 (12)			
Fe II 1373.72	3.768	58 (10)	51 (11)			
Fe II 1375.17	2.657	80 (6)	65 (12)			
Fe II 1377.99	3.814	46 (11)	< 28			
Fe II 1379.47	2.676	56 (12)	64 (10)			blend
Fe II 1379.62	1.724	44 (14)	25 (9)			blend
Fe II 1383.58	2.692	70 (7)	46 (10)			
Fe II 1387.22	2.522	55 (11)	30 (10)			
Fe II 1392.15	2.522	69 (10)	< 30			
Fe II 1392.82	2.580	93 (13)	50 (10)			
Fe II 1405.61	0.232	64 (14)	64 (12)			blend
Fe II 1408.48	2.635	68 (15)	42 (11)			
Fe II 1412.84	0.232	89 (16)	49 (12)			blend
Fe II 1413.70	2.657	62 (14)	< 30			
Fe II 1420.91	2.692	55 (14)	< 40			
Fe II 1424.72	0.301	79 (13)	55 (16)			blend
Fe II 1435.00	0.352	58 (14)	42 (13)			blend
Ni II 1317.22	0.000	126 (11)	88 (10)			
Ni II 1335.20	0.187	108 (10)	61 (9)			
Ni II 1370.13	0.000	110 (17)	85 (15)	< 6	19.7	
Ni II 1381.29	0.187	79 (10)	41 (10)			
Ni II 1393.32	0.000	43 (10)	< 30	<9.1	< 9.1	
Ni II 1411.07	0.187	63 (12)	33 (11)			

In this Table, χ is the lower energy of the observed transition, "u" means that the atomic parameters are particularly uncertain while "edge" means that the line lies very near the edge of the array. The measurements for α Vir and ζ Oph are for interstellar lines and are provided for comparison with our COS-measured values given for GD 40 and G241-6.

[a]from York & Kinahan (1979)

[b]from Morton (1975)

[c]Derived from the model fit shown in Figure 1 rather than measured directly from the data

[d]blend of S II 1204.27 Å and S II 1204.32 Å; atomic parameters from Tayal & Zatsarinny (2010)

Table 2 – Stellar Parameters			
Property	GD 40	G241-6	Reference
T_* (K)	15,300	15,300	(1), (2)
$\log g$ (cm^2 s^{-1})	8.0	8.0	(1), (2)
D (pc)	64	65	(3)

(1) Klein et al. (2010); (2) Zuckerman et al. (2010); (3) Bergeron et al. (2011)

Table 3 – Photospheric Abundances: GD 40

Z	Optical	Ultraviolet	Final
H	$-6.16^{+0.14}_{-0.20}$	$-5.1^{+0.2}_{-1.0}$	$-5.1^{+0.2}_{-1.0}$
C	...	-7.8 ± 0.2	-7.8 ± 0.20
N	<-5.3	<-8.8	< -8.8
O	$-5.61^{+0.08}_{-0.09}$	-5.68 ± 0.10	-5.62 ± 0.10
Mg	$-6.24^{+0.12}_{-0.16}$	-6.05 ± 0.10	-6.20 ± 0.16
Al	<-7.1	-7.35 ± 0.12	-7.35 ± 0.12
Si	$-6.76^{+0.07}_{-0.08}$	-6.28 ± 0.10	-6.44 ± 0.30
P	<-8.2	-8.68 ± 0.13	-8.68 ± 0.13
S	...	$-7.8: \pm 0.20$	$-7.8: \pm 0.20$
Cl	...	<-9.06	<-9.06
Ca	$-6.88^{+0.14}_{-0.22}$	-7.37 (0.20)	-6.9 ± 0.2
Ti	$-8.61^{+0.13}_{-0.20}$	...	$-8.61^{+0.13}_{-0.20}$
Cr	$-8.31^{+0.12}_{-0.16}$	...	$-8.31^{+0.12}_{-0.16}$
Mn	$-8.62^{+0.13}_{-0.18}$	-8.73 ± 0.10	-8.64 ± 0.14
Fe	$-6.48^{+0.09}_{-0.12}$	-6.46 ± 0.10	-6.47 ± 0.12
Ni	$\leq$-7.7	-7.84 ± 0.26	-7.84 ± 0.26
Cu	...	<-9.91	<-9.91
Ga	...	<-10.8	<-10.8
Ge	...	<-10.2	<-10.2

Abundances are given $\log[n(\mathrm{Z})/n(\mathrm{He})]$.

Table 4 – Photospheric Abundances: G241-6

Z	Optical	Ultraviolet	Final
H	<-6.1	-5.9 ± 0.3	-5.9 ± 0.3
C	...	<-8.5	<-8.5
N	...	<-8.9	<-8.9
O	-5.6 ± 0.10		-5.64 ± 0.11
Mg	-6.29 ± 0.05	-6.14 ± 0.10	-6.26 ± 0.10
Al	<-7.0	<-7.7	<-7.7
Si	-6.78 ± 0.06	-6.55 ± -0.10	-6.62 ± 0.20
P	...	-9.04 ± 0.13	-9.04 ± 0.13
S	...	-7.07 ± 0.28	-7.07 ± 0.28
Cl	...	<-9.2	<-9.2
Ca	-7.25 ± 0.07	-7.9 (0.2)	-7.3 ± 0.20
Ti	-8.97 ± 0.04	...	-8.97 ± 0.10
Cr	-8.46 ± 0.05	...	-8.46 ± 0.10
Mn	-8.8 ± 0.10	-8.74 ± 0.10	-8.76 ± 0.20
Fe	-6.76 ± 0.06	-6.86 ± 0.10	-6.82 ± 0.14
Ni	< -7.5	-8.15 ± 0.40	-8.15 ± 0.40
Cu	...	<-9.90	<-9.90
Ga	...	<-10.8	<-10.8
Ge	...	<-10.2	<-10.2

Abundances are given as $\log[n(Z)/n(He)]$.

Table 5 – Mixing-Zone Masses

Z	GD 40 (10^{21} g)	G241-6 (10^{21} g)
H	3.4	0.54
C	0.081	<0.016
O	16	16
Mg	6.5	5.7
Al	0.51	< 0.23
Si	4.3	2.9
P	0.027	0.012
S	0.22:	1.2
Ca	2.1	0.85
Ti	0.050	0.022
Cr	0.11	0.077
Mn	0.055	0.041
Fe	8.0	3.6
Ni	0.36	0.18
Total	38	31

We assume the total mass of the outer convection zone is 1.7×10^{27} g (Klein et al. 2010). The value for the "Total" mass of pollutants in the mixing zone excludes hydrogen because some of this element may be primordial (Bergeron et al. 2011) or it may have been accreted in previous episodes. The mass fraction of each individual element is derived by computing the ratio of its mass to that of the "Total"; the results are displayed in Figures 11-13. The correspondence between the mass fractions of pollutants in the stellar atmosphere and the bulk composition of the accreted parent body is discussed in Section 4.
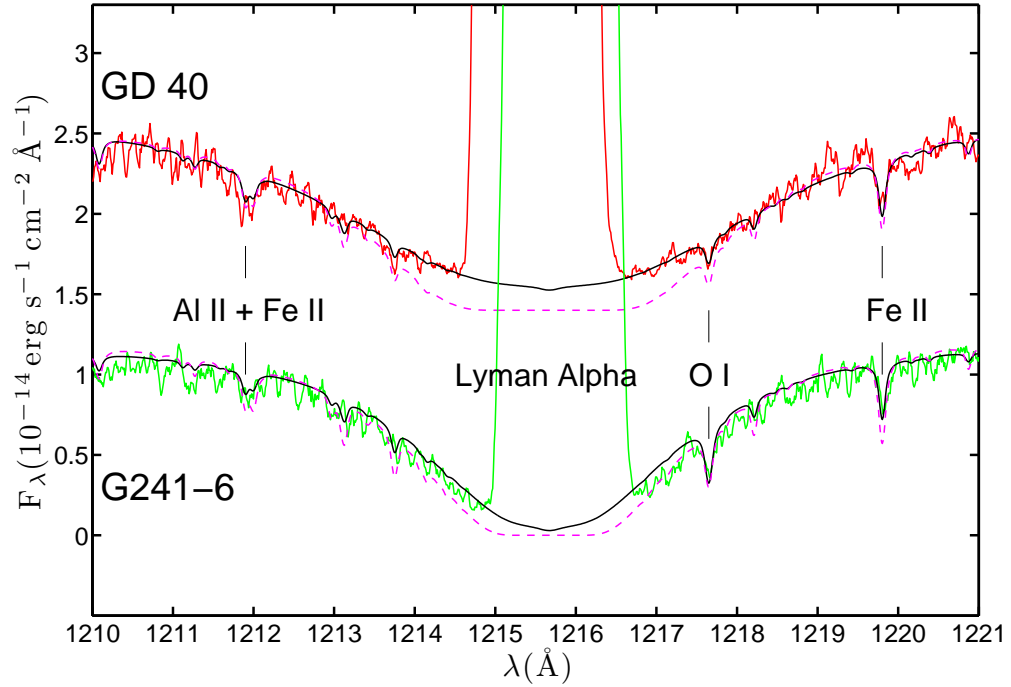
Fig. 1.— Lyman α absorption in GD 40 and G241-6. The black lines represent models with the "final" abundances given in Table 3 and 4 without any interstellar contribution. The dashed pink lines represent models with [H]/[He] = -6.16 and column densities of interstellar hydrogen of 1×10^{20} cm^{-2} and 3×10^{19} cm^{-2} toward GD 40 and G241-6, respectively (see Section 3.2). For clarity, the spectrum for GD 40 is offset by 1.5×10^{-14} erg s^{-1} cm^{-2} Å^{-1}. Because the data are shifted into the star's frame of reference, the dayglow emission lines for the two stars are displaced.
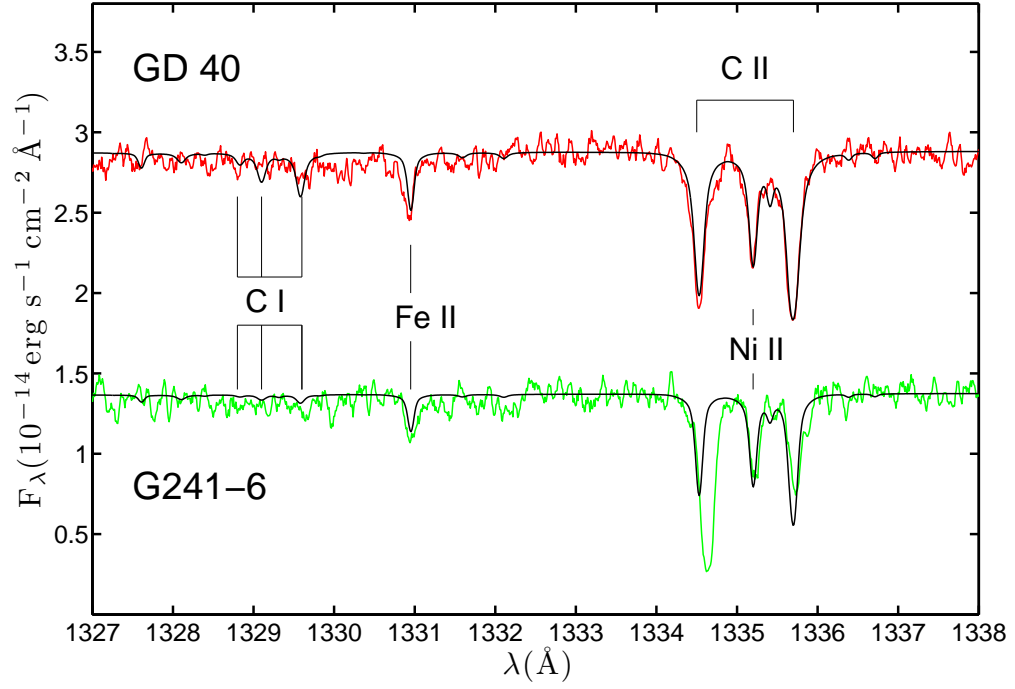
Fig. 2.— Similar to Figure 1 except for C I and C II. For G241-6, the C II line at 1334.53 Å is shifted by +19 km s^{-1} with respect to the photospheric velocity; likely it is largely interstellar. We regard the C I lines to be undetected in both stars.
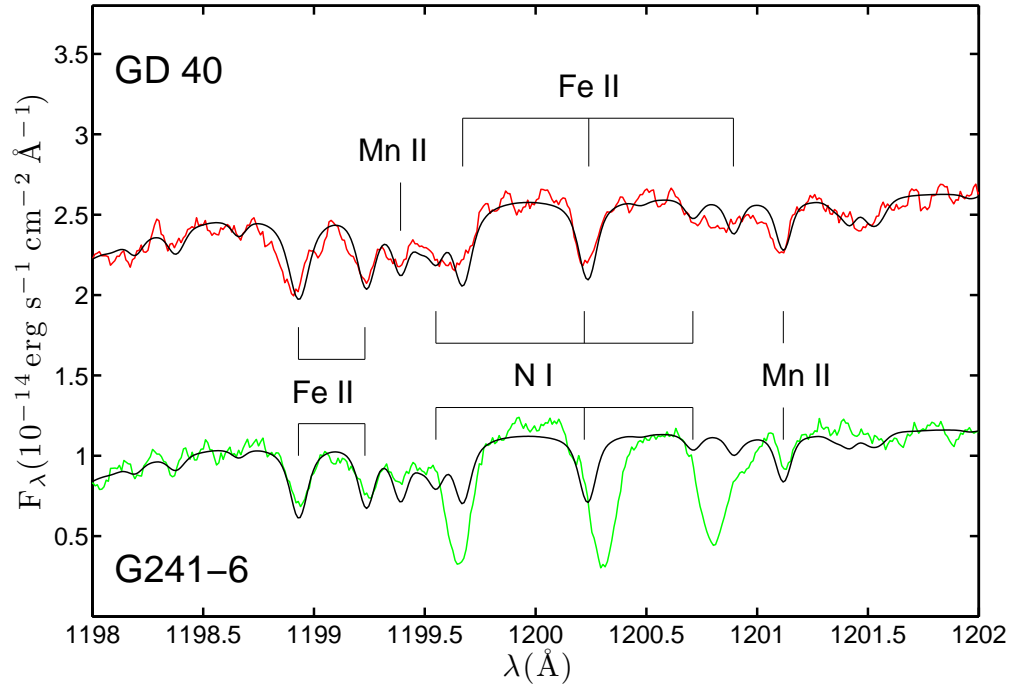
Fig. 3.— Similar to Figure 1 except for the spectral region near prominent N I lines. For G241-6, the N I lines at 1199.55 Å, 1220.22 Å and 1200.71 Å are shifted by +26 km s^{-1}, +21 km s^{-1} and +26 km s^{-1}, respectively, relative to the photospheric velocity. These N I lines likely are interstellar. For GD 40, the lines from Fe II at 1199.67 Å, 1200.24 Å and 1200.75 Å dominate in the model spectrum, and there is no evidence for any photospheric nitrogen.
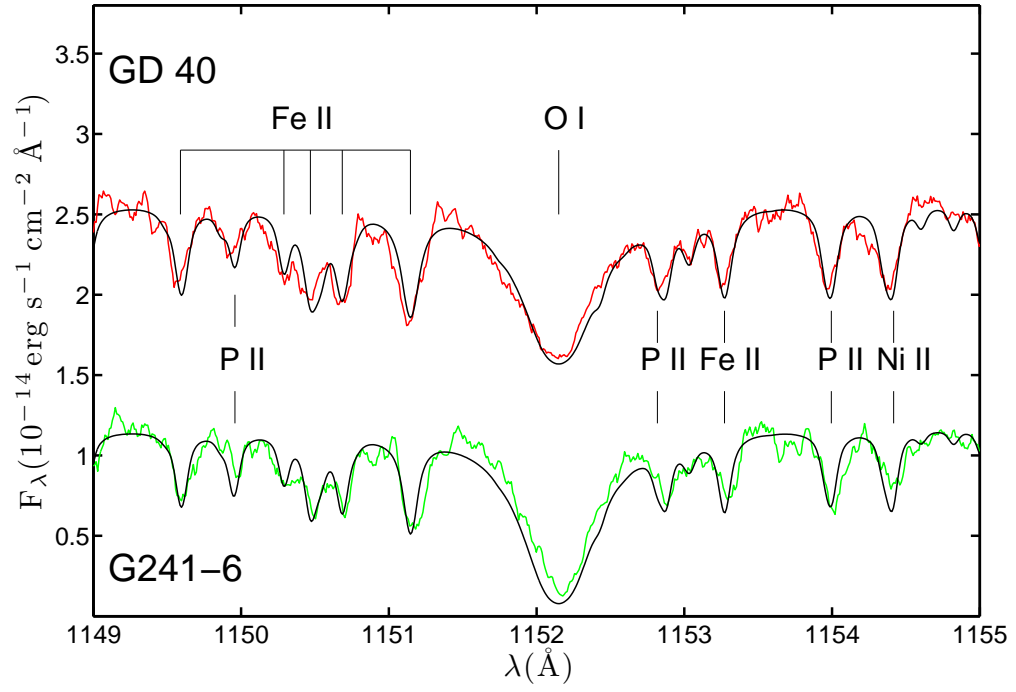
Fig. 4.— Similar to Figure 1 except for the O I line at 1152.15 Å as well as lines of P, Fe and Ni.
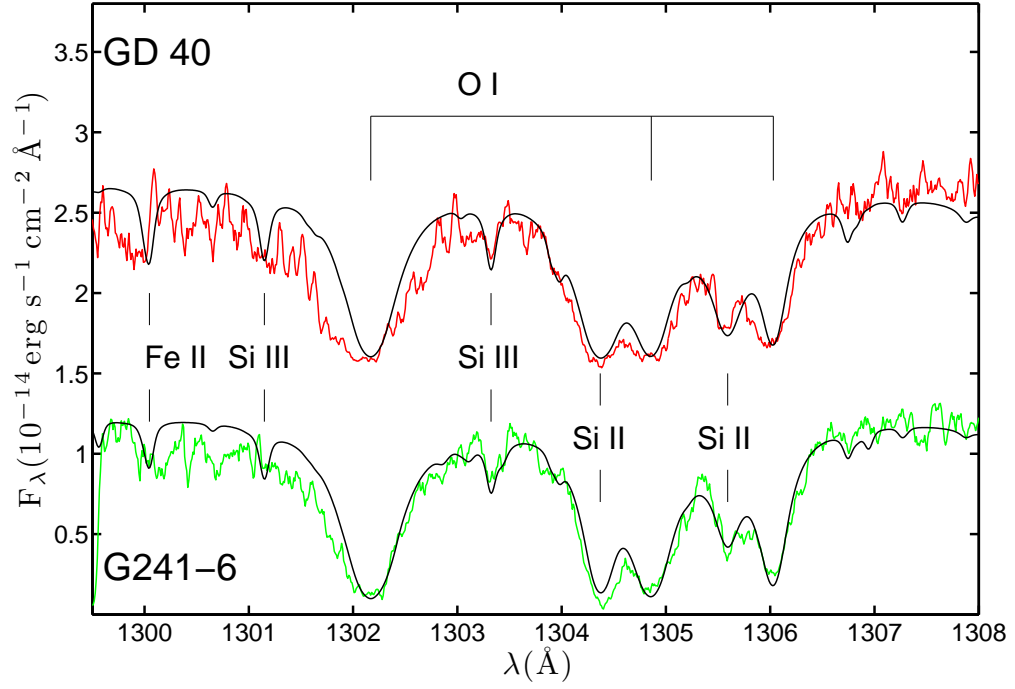
Fig. 5.— Similar to Figure 1 except for the O I lines at 1302.17 Å, 1304.86 Å and 1306.83 Å as well as lines of Fe and Si. These are "night time" data and therefore we have less exposure time on-source and a lower signal-to-noise ratio in the data.
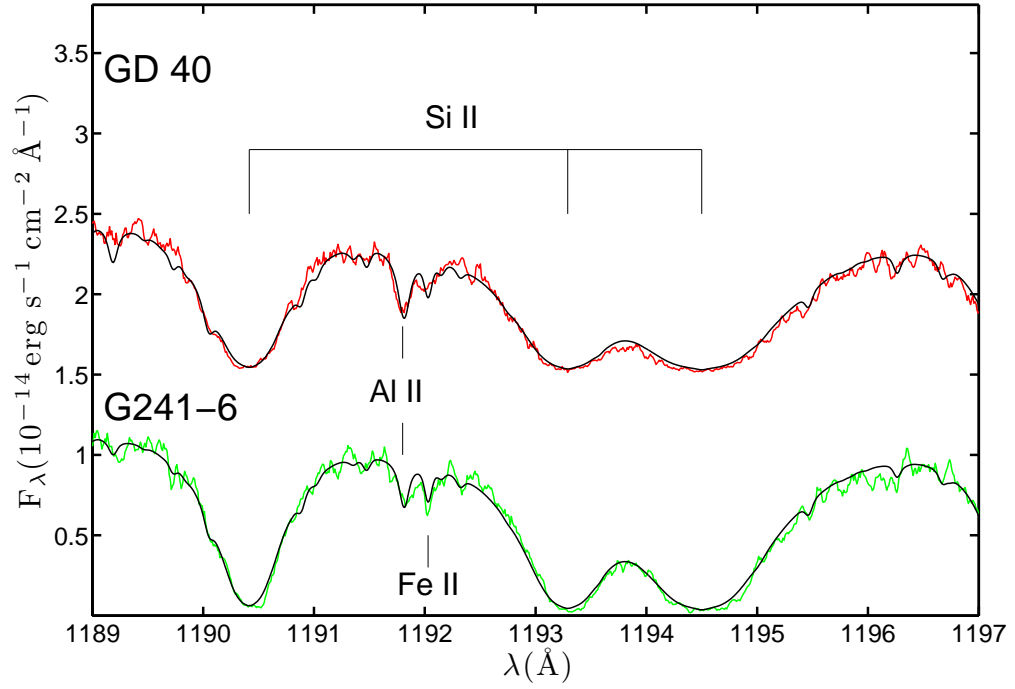
Fig. 6.— Similar to Figure 1 except for the spectral region near the Al II line at 1191.8 Å. In GD 40, the aluminum line is stronger than the adjacent iron line; in G241-6, the aluminum line, if real, is weaker than the adjacent iron line. Because iron is more abundant in GD 40 than in G241-6, these spectra directly demonstrate that aluminum is substantially more abundant in GD 40.
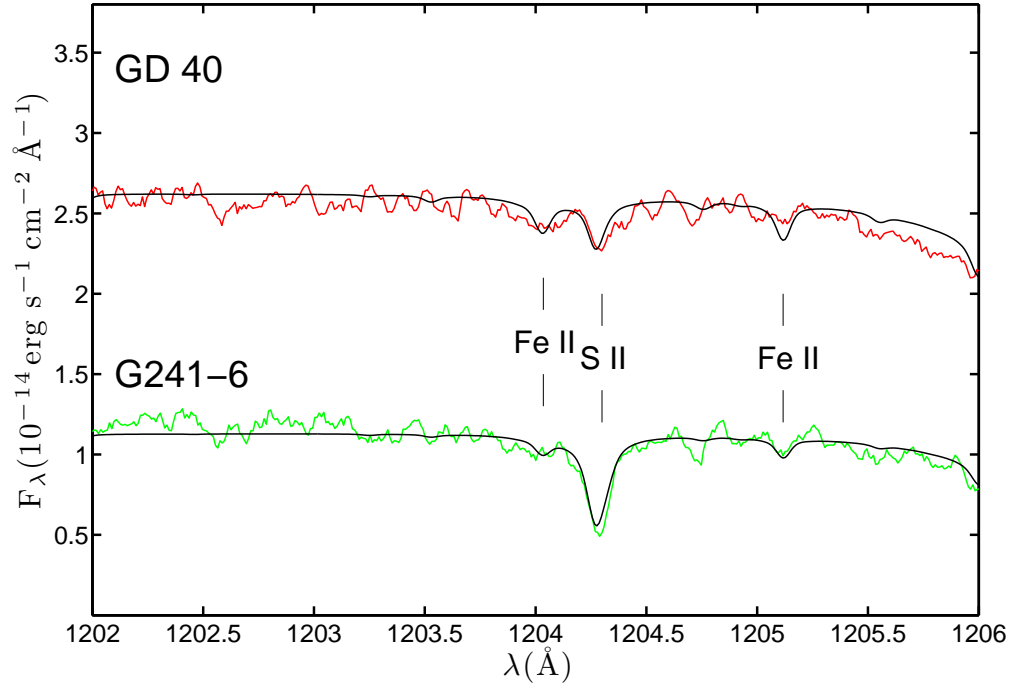
Fig. 7.— Similar to Figure 1 except for the spectral region near the S II doublet at 1204.27 Å and 1204.32 Å.
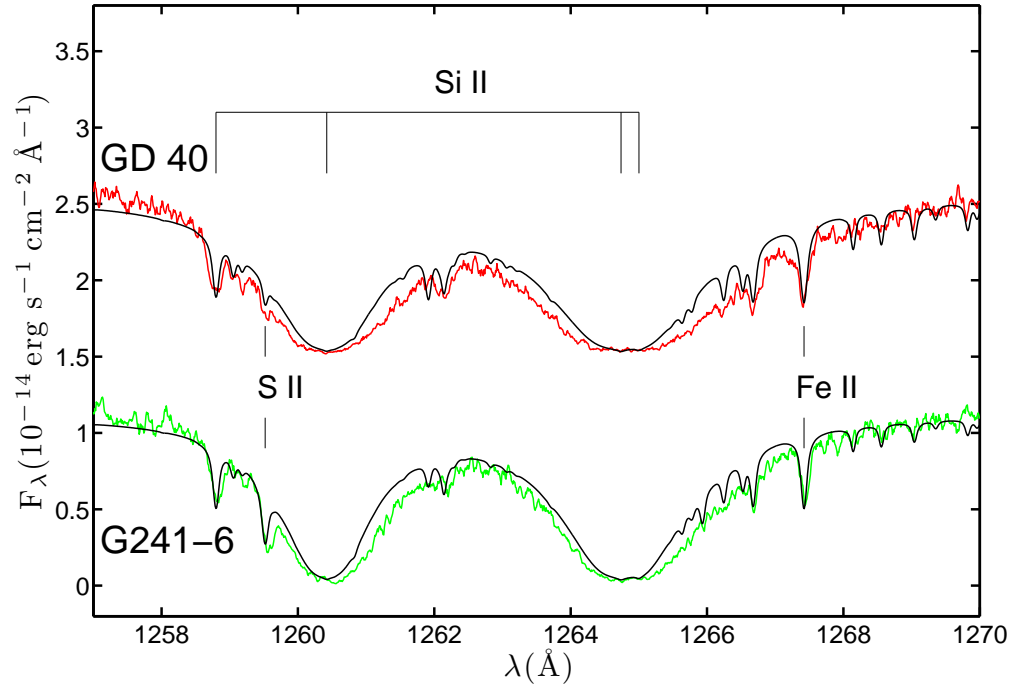
Fig. 8.— Similar to Figure 1 except for the spectral region near the Si II lines near 1260 Å.
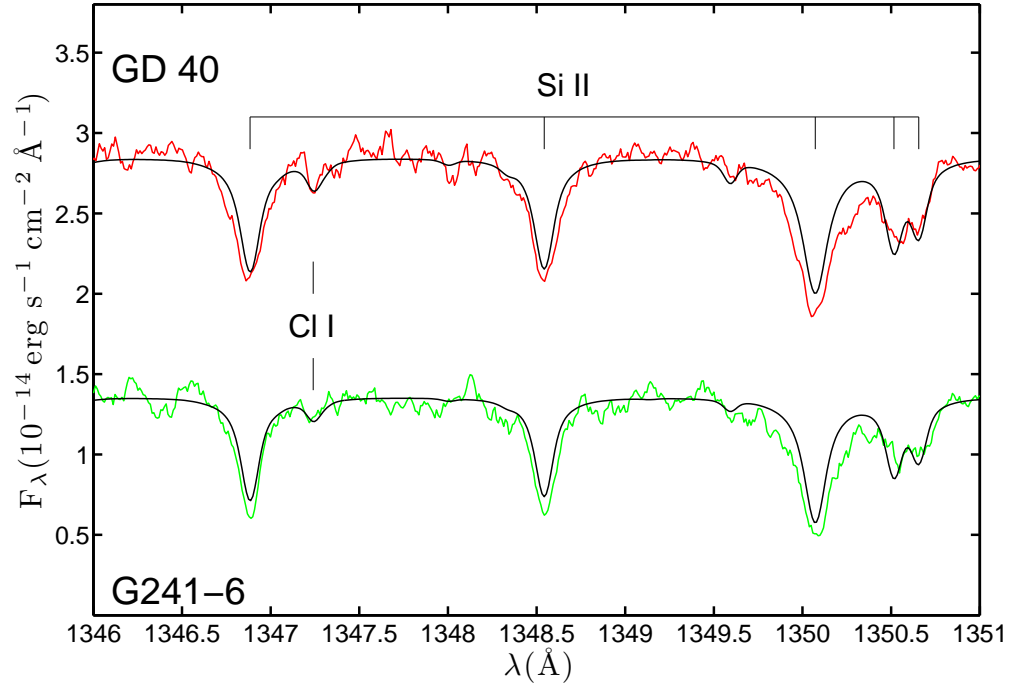
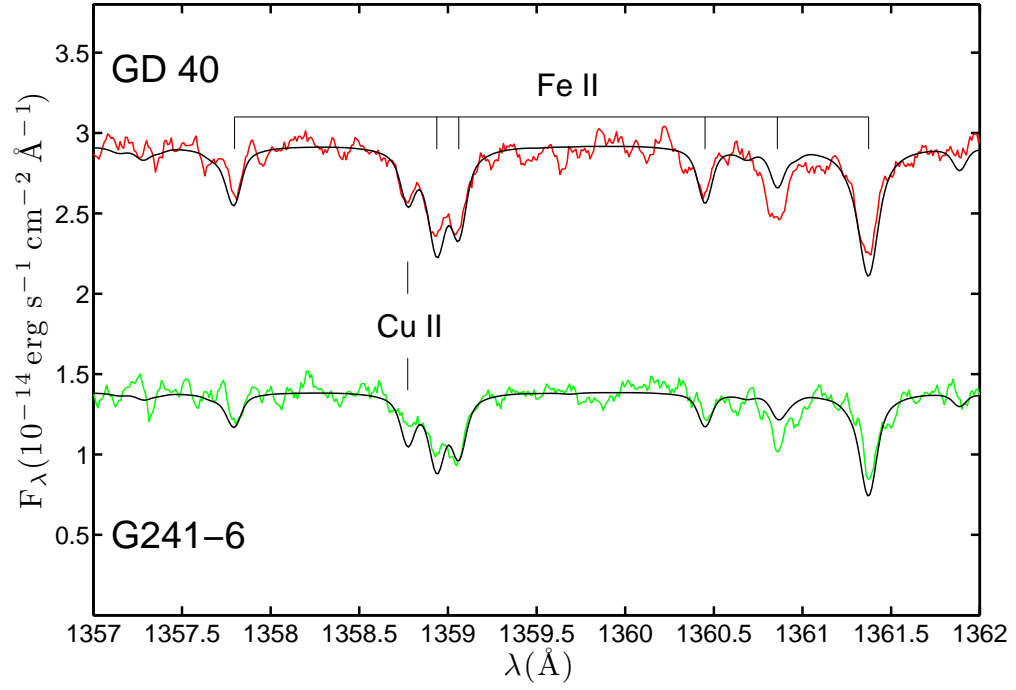Fig. 9.— Similar to Figure 1 except for the spectral region near the undetected Cl I line at 1347.24 Å

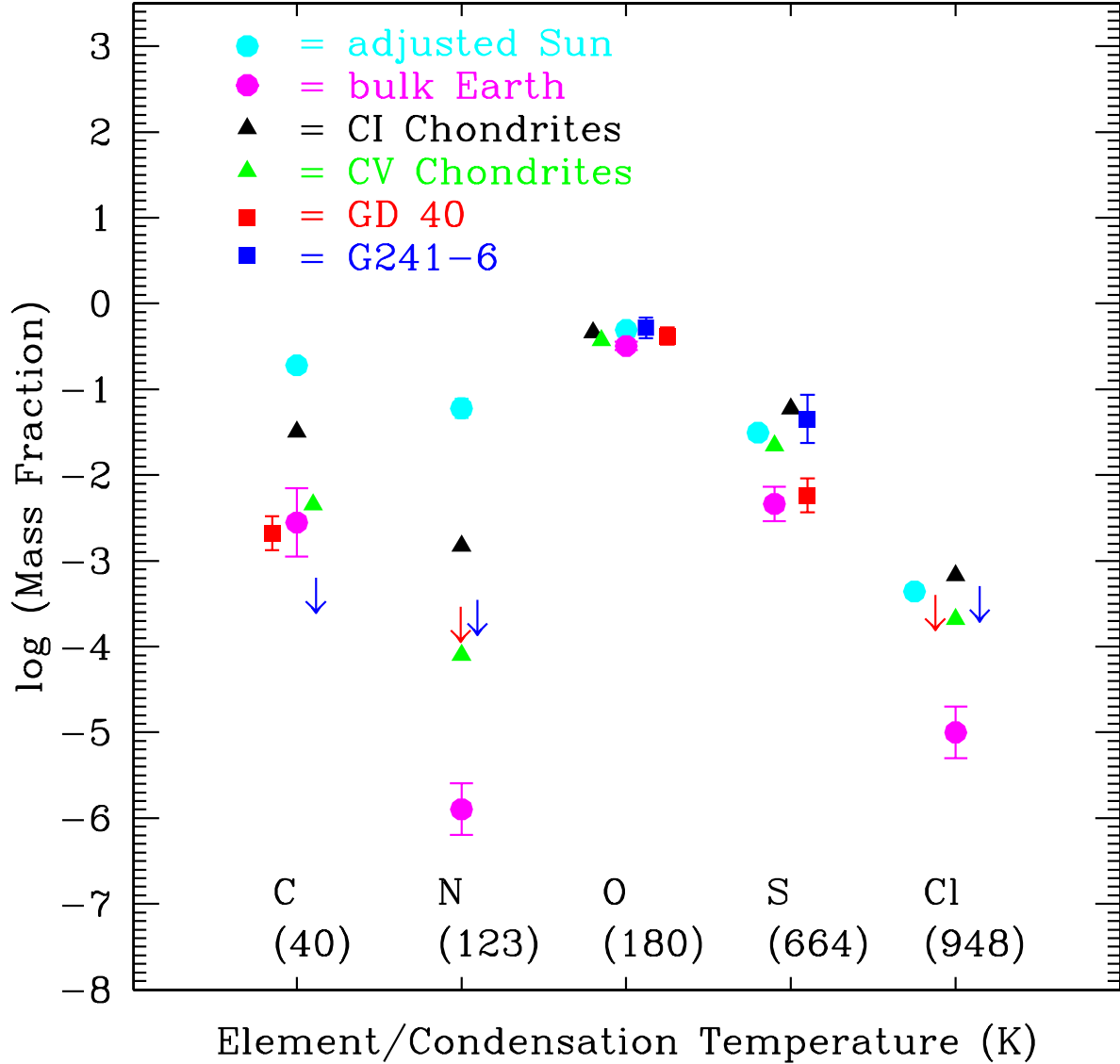Fig. 10.— Similar to Figure 1 except for the spectral region near the undetected Cu II line at 1358.77 Å.

Fig. 11.— Display of results tabulated in Table 4: mass fractions of elements with 50% condensation temperatures less than 1000 K in the parent bodies accreted onto GD 40 and G241-6 and, for comparison, both CI and CV chondrites (Wasson & Kallemeyn 1988), bulk Earth (Allegre et al. 2001) and an "adjusted Sun" which is all elements except hydrogen, helium and the noble gases given by Lodders (2003). The temperature at which 50% of the element condenses in the calculations of Lodders (2003) is shown beneath its symbol on the plot. The relationship between the mass fractions of pollutants in the stellar atmosphere and the bulk composition of the accreted parent body are discussed in Section 4. To make a conservative estimate of the mass fraction of the important volatiles – carbon, nitrogen and oxygen – we assume the system is in the build-up phase. If the system is in a steady state or declining phase, then the results plotted here overestimate the mass fractions of the lighter elements and underestimate the mass fractions of the heavier elements in the parent bodies.
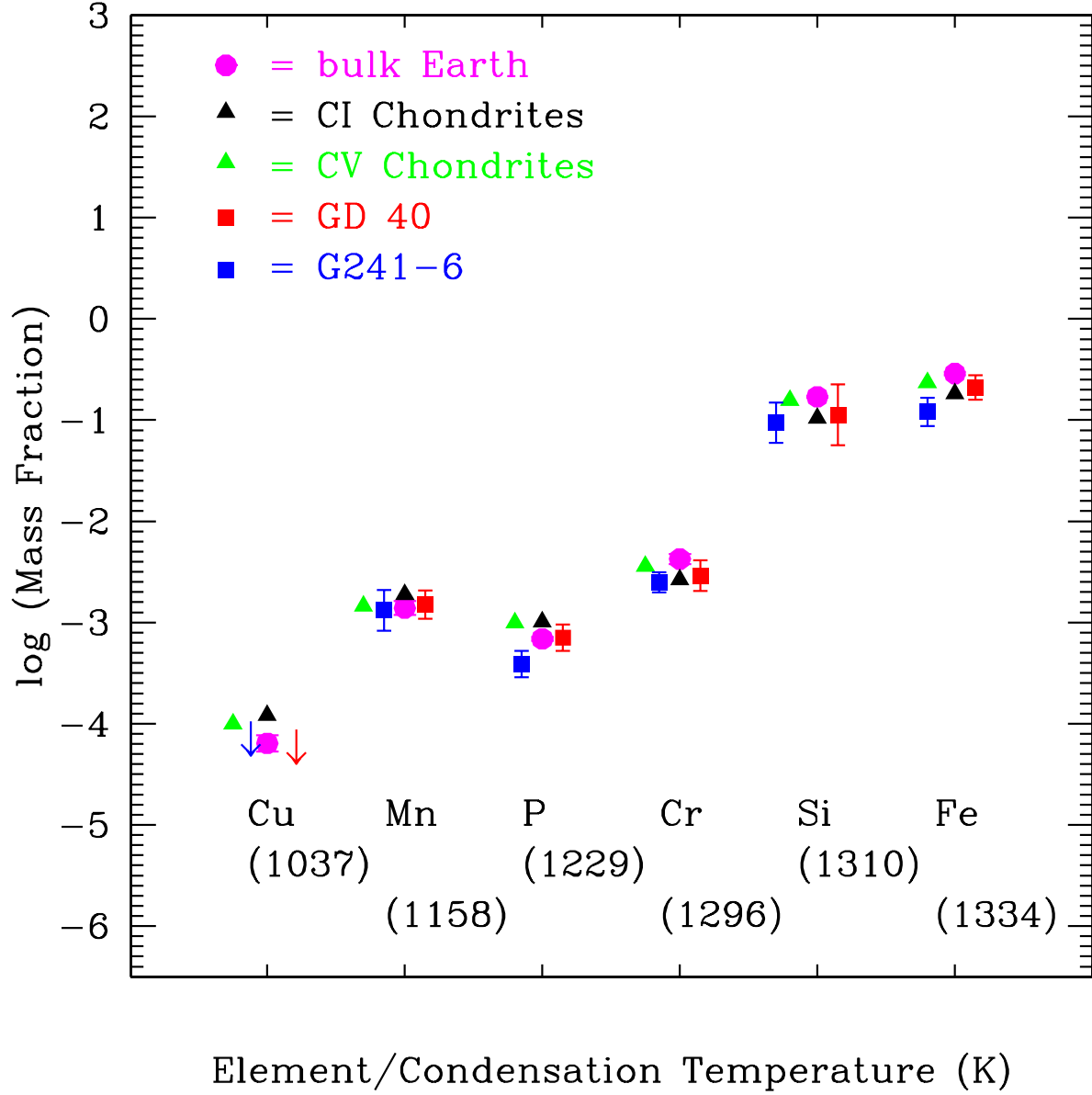
Fig. 12.— Similar to Figure 11 for elements with condensation temperatures greater than 1000 K and less than 1335 K. We do not display "adjusted Sun" because it has the same pattern as "CI Chondrites".
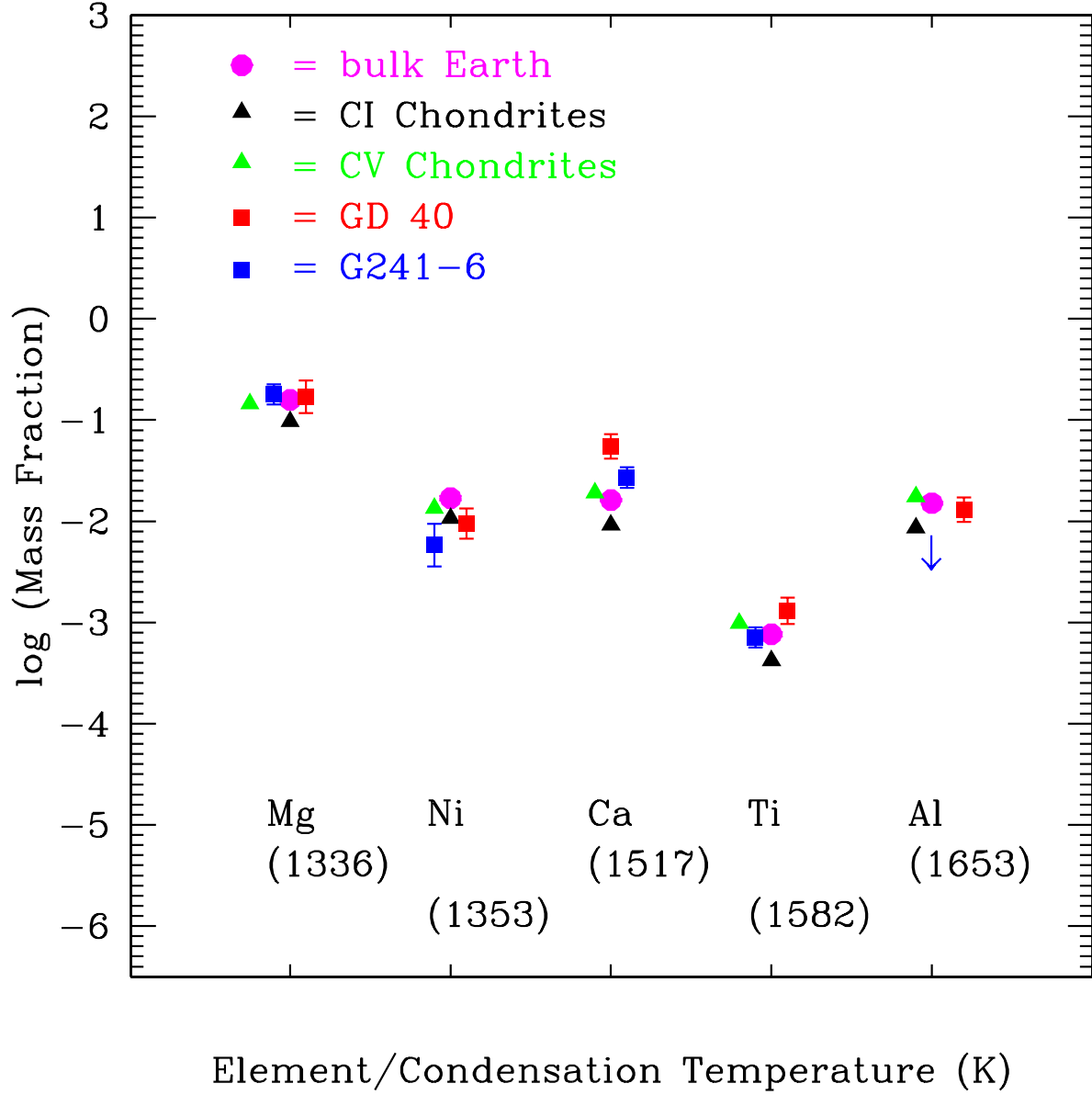
Fig. 13.— Similar to Figure 11 for elements with condensation temperatures greater than 1335 K. We do not display "adjusted Sun" because it has the same pattern as "CI Chondrites".